CrossMark

ORIGINAL ARTICLE

# Effect of static magnetic field on microstructures and mechanical properties of laser-MIG hybrid welding for 304 stainless steel

Rong Chen[1] · Ping Jiang[1] · Xinyu Shao[1] · Gaoyang Mi[2] · Chunming Wang[2]

**Abstract** In this study, a method combining magnetic, MIG, and laser was applied to weld the 304 stainless steel with a thickness of 4 mm. The effect of magnetic field on the weld microstructures and mechanical properties was investigated. The weld geometry and microstructure were characterized by optical microscope (OM) and scanning electric microscopy. Electron back scattered diffraction (EBSD) was used to determine the grain sizes and crystallographic orientations. Residual stress and tensile stress of welds were measured and compared with the laser-arc hybrid welds without an external magnetic field. The results showed that with an appropriate magnetic field intensity, an optimal joint was obtained with tensile strength enhanced by nearly 12% and tensile residual stresses reduced. In addition, the grain refining and promotion of the phase transformation with the magnetic field were analyzed.

**Keywords** Magnetic field · Laser-MIG hybrid welding · Hardness measurement · Residual stress · Electron back scattered diffraction

✉ Ping Jiang
jiangping@hust.edu.cn

[1] The State Key Laboratory of Digital Manufacturing Equipment and Technology, School of Mechanical Science and Engineering, Huazhong University of Science & Technology, 430074 Wuhan, People's Republic of China

[2] School of Materials Science and Engineering, Huazhong University of Science & Technology, 430074 Wuhan, People's Republic of China

## 1 Introduction

The electromagnetic processing of materials (EPM) has aimed to design efficient processes by making the best of various functions appearing between the electric and magnetic fields. Asai et al. [1] summarized that the EPM has often combined two channels including metallurgy and magnetohydrodynamics. In the past decades, the electromagnetic force (EMF), which had significant effects on the melt flow conditions and arc behaviors, has been widely used in arc and laser welding to improve the weld quality [2–5]. Bachmann et al. [6] found that the dropout due to the hydrostatic pressure was prevented by the application of AC magnetic field during the laser welding process. Liu et al. [3] showed that the axial external magnetic field with alternating magnetic induction and frequency changed the weld microstructure and mechanical properties during the cold metal transfer welds of aluminum and stainless steel. Mousavi et al. [7] suggested that the electromagnetic stirring effect during arc-magnetic welding promoted the grain detachment and acted as an important factor for nucleation and grain refinement. Bachmann et al. [8] pointed out that the longitudinal static magnetic field applied during laser welding broke the flow velocity and changed the local temperature distribution in the weld pool. Overall, the application of a magnetic field during laser or arc welding has an effect on the energy distribution and melt flow conditions and then affected the microstructure of welded joints, which resulted in a variation of the properties, like mechanical property and corrosion property.

Taking advantages of the laser beam and electric arc, hybrid welding has acquired many values in recent years [9–12]. It offers remarkable superiorities over laser welding and arc welding alone. Bagger and Olsen [13] presented an overview on the merits and demerits of laser-arc hybrid welding based on the industrial applications. It was reported in the review

that the hybrid welding had a higher welding speed, deeper penetration, better weld quality, preferred gap bridging ability, and good process stability and efficiency. Liu et al. [14] proved that a desired wineglass-shaped weld was obtained with appropriate process parameters during laser-arc welding of 10 mm thick superalloy GH909. In Europe and Asia, hybrid welding has been applied widely in a number of different industries, including automotive welding, shipbuilding, pipelines, and railcar industries. However, Bagger and Olsen [13] pointed out that the application of hybrid welding technique means extra amount of heat added to the material compared to conventional arc welding or pure laser welding. The welding speed must be increased proportionally to the increase in energy, or the heat input per welded length will be added. It is critical to coordinate between the heat input and the welding speed. On one hand, the welding joints will be filled of coarser grains as well as larger heat affected zones if the welding rate is controlled below the most appropriate value. On the other hand, the welds are susceptible to pores and microstructural heterogeneity with a faster welding and cooling speed. Therefore, to solve these problems, an electromagnetic field was introduced into the hybrid welding in this study to control the flow of molten metal by means of the synergistic effect between the magnetic field and the electric field.

Previous studies mainly focused on effects of the magnetic field during arc or laser welding alone, but the effects during laser-metal inert gas (MIG) hybrid welding process have not been reported. However, the concept of the magnetic field coupling with laser-MIG hybrid welding is much more attractive for the combination of the advantages of magnetic processing with the superiorities of hybrid welding. This experimental research on the magnetic-MIG-laser welding system will contribute to the analysis of the internal interaction among magnetic field, laser, and the electric field. Considering that the adhibition of a magnetic field is contactless and the exertion of pulsed electric current during the welding is extremely neat, it is suitable for actual application environment. Moreover, the controlling configuration with regard to electric current and magnetic field has obtained a rapid development in recent years. The application of magnetic field during arc-laser welding is proved to be a financial and efficient method to optimize laser-arc hybrid welding process.

This paper discussed the effect of external magnetic field on the microstructure and mechanical properties during MIG-laser welding systematically, which had hardly been conducted before. In the present study, an external static magnetic field of 8–32 mT is utilized during MIG-laser hybrid welding SUS304 austenite stainless steel. The magnetic field intensity was set as a single variable to study its effect on the weld-bead shape, microstructure, and phases in the joints. Then, the tensile strength, microhardness, and residual stress of samples were tested to reveal the relevance between microstructure and mechanical properties. As the improvement of a

24-mT magnetic field on the tensile strength was the most apparent, this study is mainly focused on the differences of microstructures and mechanical properties between the 0 and 24 mT samples.

## 2 Experimental procedures

### 2.1 Materials

The experimental materials were SUS304 alloy of 4 mm in thickness and austenitic stainless steel ER 316L filler wire with 1.2 mm in diameter. The chemical compositions are shown in Table 1. Before welding, the sheets were cleaned by grinding wheel. Acetone solute was used to remove oxidation film and greasy on the surface of the substrates. In order to protect the welding joints from being oxidized during the process, mixture gas of argon and carbon dioxide (80% Ar + 20% $CO_2$) with a flow rate of 1.5 m³/h was employed as the shielding atmosphere.

### 2.2 Welding procedure

A 4-kW fiber laser (IPGYLR-4000) was used for a bead-on-plate weld. The fiber laser can deliver in continuous wave mode with a 1.07-μm emission wavelength. The laser beam is focused as a spot with a 0.3-mm diameter on the plates. A Fronius TPS 4000 digital arc power was used as the MIG welding power controller. During welding, a rectangular pulsed direct current with 160 A as the maximum value was used. The external magnetic field was produced by a permanent magnet with a dimension of 100 mm × 100 mm × 20 mm setting under the jig and fixture while the maximum width of the welding bead was nearly 5 mm. As the size of the molten pool was so small comparing with the dimensions of the magnet, the distribution of the magnetic induction lines along the welding direction could be supposed to be homogeneous and pass through the molten pool vertically. Accurate intensity of magnetic field in center of the weld pass was pre-measured before welding by a high-precision gauss meter. The magnetic induction intensity was adjusted by changing distance between the magnet and welding plate. The schematic of the setup is shown in Fig. 1. During experiments, magnetic field intensity was the single variable parameter and the others were kept unchanged according to Table 2.

### 2.3 Cross-section analysis

After welding, samples were cut from center of the weld to match the exact magnetic intensity measured before. The metallographic specimens were grinded and polished, and then etched using an etchant consisting 15 mL hydrochloric acid

**Table 1** Chemical compositions of base metal and filler wire (wt.%)

| Element | C | Si | Mn | P | S | Cr | Ni | N | Mo |
|---------|-----|-----|---------|------|-------|-----------|-----------|------|--------|
| SUS 304 | 0.05 | 0.46 | 1.15 | 0.03 | 0.001 | 18.01 | 8.01 | 0.05 | 0.0459 |
| ER 316L | ≤0.03 | ≤0.6 | 1.0–2.5 | ≤0.03 | ≤0.02 | 18.0–20.0 | 11.0–14.0 | – | 0.2–3.0 |

and 5 mL nitric acid. An optic microscope (OM) and a scanning electron microscopy were applied to observe the geometry morphologies and microstructures of the welded joints. Energy-dispersion X-ray (EDX) analyses were used to identify different phases. Phase constituents on the transverse section of the specimens were determined by X-ray diffraction (XRD) using CuKα radiation. The diffraction angle ($2\theta$) represented the hitting angles of X-rays on the samples varied from 30° to 90°, with a step size of 0.05° and stayed 2 s in a step.

## 2.4 Samples preparation for EBSD measurements

Electron backscatter diffraction (EBSD) method was used to determine the grain sizes and crystallographic orientations. As principle of the EBSD is to explore the information collected from backscattered electrons emitted from the surface of the specimen, the sample was inclined 70° relative to the incident beam, so that the back-scattering signal electron backscatter pattern (EBSP) is sufficient in strength to be received by the fluorescent screen. Thus Kikuchi pseudo-bands were drawn on the screen. The corresponding crystallographic orientations and grain sizes were calculated utilizing the OIM software according to the Kikuchi patterns. To get precise data analysis, residual stress and deformation brought by the mechanical treatment must be removed. Firstly, the specimen were grinded by abrasive paper up to 2000 mesh and then polished with 1.5 μm diamond polishing paste. After that, the electrochemical polishing was conducted at 25 °C in 10% perchloric acid and 90% ethyl alcohol for 45 s to remove the residual stress on the surface. Finally, the

specimens were cleaned by ultrasonic wave method. In order to protect from the contamination, the specimens were immersed in acetone before tests. During the EBSD test, a dimension of 645 μm × 200 μm at center of the plate near the fusion line were chosen as the explored area and the acquisition step were 1.8 μm.

## 2.5 Measurement of residual stresses, tensile stresses, and hardness

Transverse tensile strength tests were conducted using a Universal Material Testing Machine according to ASTM A370-14 standard. Residual stresses in the 24 and 0 mT joints were measured using X-ray diffraction technique basing on Bragg's law. The X-ray source was CrK$_\beta$ with 25 kV voltage. The diffraction plane was (311) plane for austenite and the scanning angle ranged from 125° to 156°. In order to ensure data accuracy, the lattice spacing $d$ was measured at four $\Psi$ angles: 0°, 25°, 35°, and 45°. The residual stress was evaluated based on the variations of $2\theta$ versus $\sin^2 \Psi$ plots. As the degree of accuracy is closely related with the test surface roughness, the metal above the test plane and the test surface were treated with electrochemical polishing before measurement. Hardness measurements were conducted along line 1 as indicated in Fig. 2. Line 1 was 1 mm away from the upper boundary of the plate. Distance between the test points was 200 μm and the loading duration was 15 s. The samples were polished to avoid porosity on the surface before test. In order to determine the extent of heat-affected zone (HAZ) during the testing, the samples were slightly etched before test.

**Fig. 1** **a** Schematic of laser-arc-magnet welding of steel. **b** Optical image of the configuration
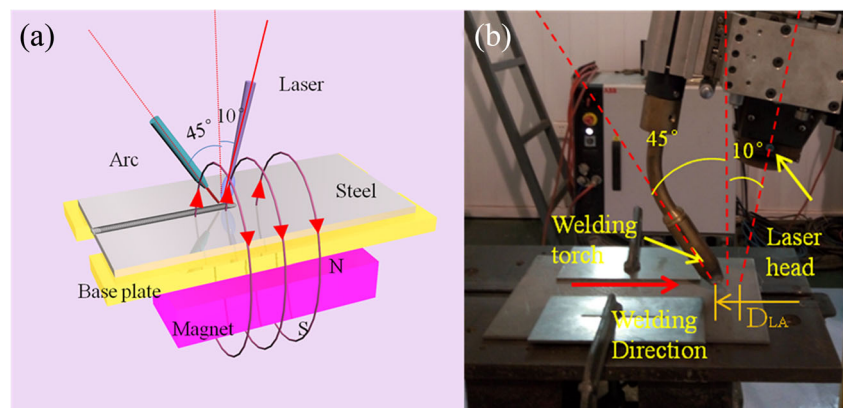
**Table 2** Process parameters

| Test | Power (kW) | Velocity (m/min) | Defocusing distance (mm) | Gas flow (m³/h) | Magnetic intensity (mT) | Pulse current (A) | Wire feeding speed(m/min) |
|---|---|---|---|---|---|---|---|
| Control group | 3.2 | 1.6 | −1 | 1.5 | 0 | 160 | 5.3 |
| Experiment group | 3.2 | 1.6 | −1 | 1.5 | 0–32 | 160 | 5.3 |

# 3 Results

## 3.1 Morphology and defect observation

Weld appearance of the welded joint is an important factor determining the adhesion area and melt metal distribution. Shapes of hybrid welded samples obtained with magnetic field and the referring samples without magnetic field are shown in Fig. 3. It was observed that the welding width was increased and the sagging metal was reduced with an 8–32-mT magnetic field.

## 3.2 Microstructure analysis

The typical microstructure of the weld center and regions near the fusion line is exhibited in Fig. 4. According to the EDX results in Fig. 4, Cr content was higher in A than B and Ni content was higher in B than A, which means that the welded joints were composed of a majority of γ-austenite with minor δ-ferrite precipitated near the boundary. It was shown that δ-ferrite was distributed in strip form near the fusion line. δ-ferrite was much coarser in the 0 mT sample than 24 mT sample both in weld center and in regions near the fusion line.

EBSD measurements were carried out at region A which is located in center of the plate as it indicated in Fig. 2. Each individual grain was color coded on the basis of the crystallographic surface normal vector. Crystallographic orientations of grains in HAZ were anisotropic. As welding direction was vertical to the figure plane, the elongated directions were marked with a white arrow in Fig. 5. It was found that the

elongated directions of columnar grains had a deviation angle with respect to the travel direction. Deviation angles of the column grains in Fig. 5b were bigger than the angles in Fig. 5a. As the growth direction was closely related to the thermal field, it was indicated that the temperature field was changed accompanied with variations on flow field via the external magnetic field. According to the results, grains grew from the base metal epitaxially and then developed into column grains in the optimal direction. The optimal <100> direction for cubic crystal remained unchanged in both cases. The epitaxial grains were slightly finer in 24 mT sample than 0 mT sample; however, grain refining mainly occurred in the period when epitaxial grains grew into columnar grains.

## 3.3 Phases analysis

Figure 6 presents the corresponding XRD pattern on the cross section of the welds. Ruud [15] proposed a direct comparison method assessing the respective volume fraction of δ-ferrite in weld of the stainless steels. The volume fraction of δ-ferrite ($C_\delta$) was counted using the following formula according to ASTM E975-03 [16]

$$C_\delta = \left[ 1 + \frac{(I_{\gamma(111)}/R_{\gamma(111)}) + (I_{\gamma(200)}/R_{\gamma(200)}) + (I_{\gamma(220)}/R_{\gamma(220)})}{1.5\left((I_{\delta(110)}/R_{\delta(110)}) + (I_{\delta(200)}/R_{\delta(200)})\right)} \right]^{-1}$$
$$= \left[ 1 + \frac{(I_{\gamma(111)}/182.8) + (I_{\gamma(200)}/81.6) + (I_{\gamma220}/44.4)}{1.5\left((I_{\delta(110)}/233.8) + (I_{\delta(200)}/31.9)\right)} \right]^{-1} \quad (1)$$

Values of $R_\gamma$ (hkl) and $R_\delta$ (hkl) of γ and δ for various planes were obtained from Jatczak [17], and the $I_\gamma$ (hkl) and

**Fig. 2** The schematic display of test locations: EBSD tests were conducted at region A. Hardness tests were conducted along *line 1*
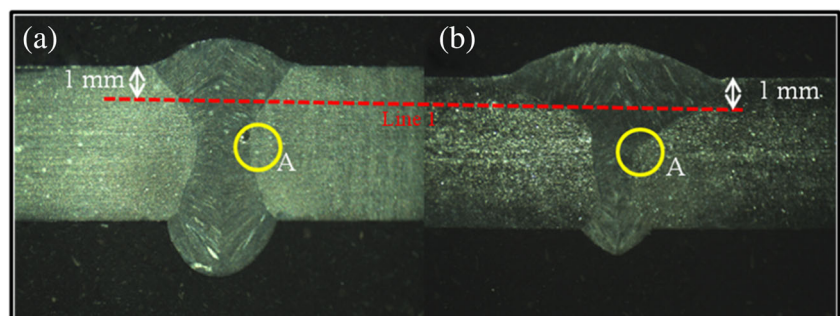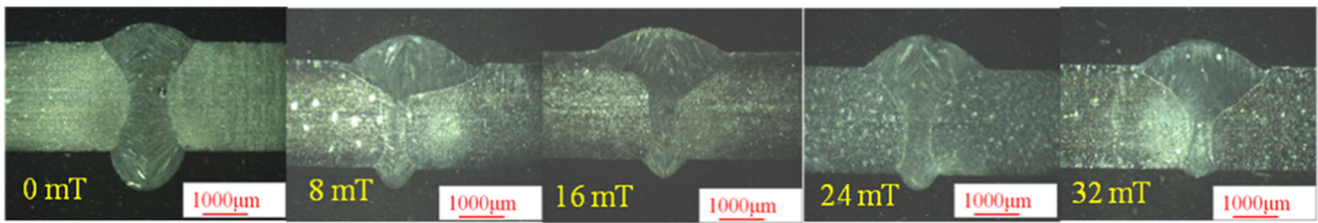
**Fig. 3** Weld geometry at different magnetic field intensity

$I_\delta$ (hkl), respectively, are the integrated intensities of a given crystallographic plane (hkl) of the $\gamma$ and $\delta$ phases.

Volume fractions of the δ-ferrite of various welds were calculated using Eq. (1) based on the XRD spectra. The spectra together with the calculation results were displayed in Fig. 6. Comparing with the referring experiments without magnetic field, the intensity of δ-ferrite decreased as magnetic field was 8–32 mT.

### 3.4 Tensile property

Molak [18] stated that a static uniaxial tensile test can get the decisive strength parameters as ultimate tensile strength (UTS). Tensile test reflects the capacity of specimens to resist elastic deformation, plastic deformation, and fracture under an increasing load. In this experiment, tensile test was conducted

**Fig. 4** Microstructures in weld center: **a** 0 and **b** 24 mT samples. EDX results of phases: *A* for ferrite and *B* for austenite. Microstructures near the fusion line: **c** 0 and **d** 24 mT samples
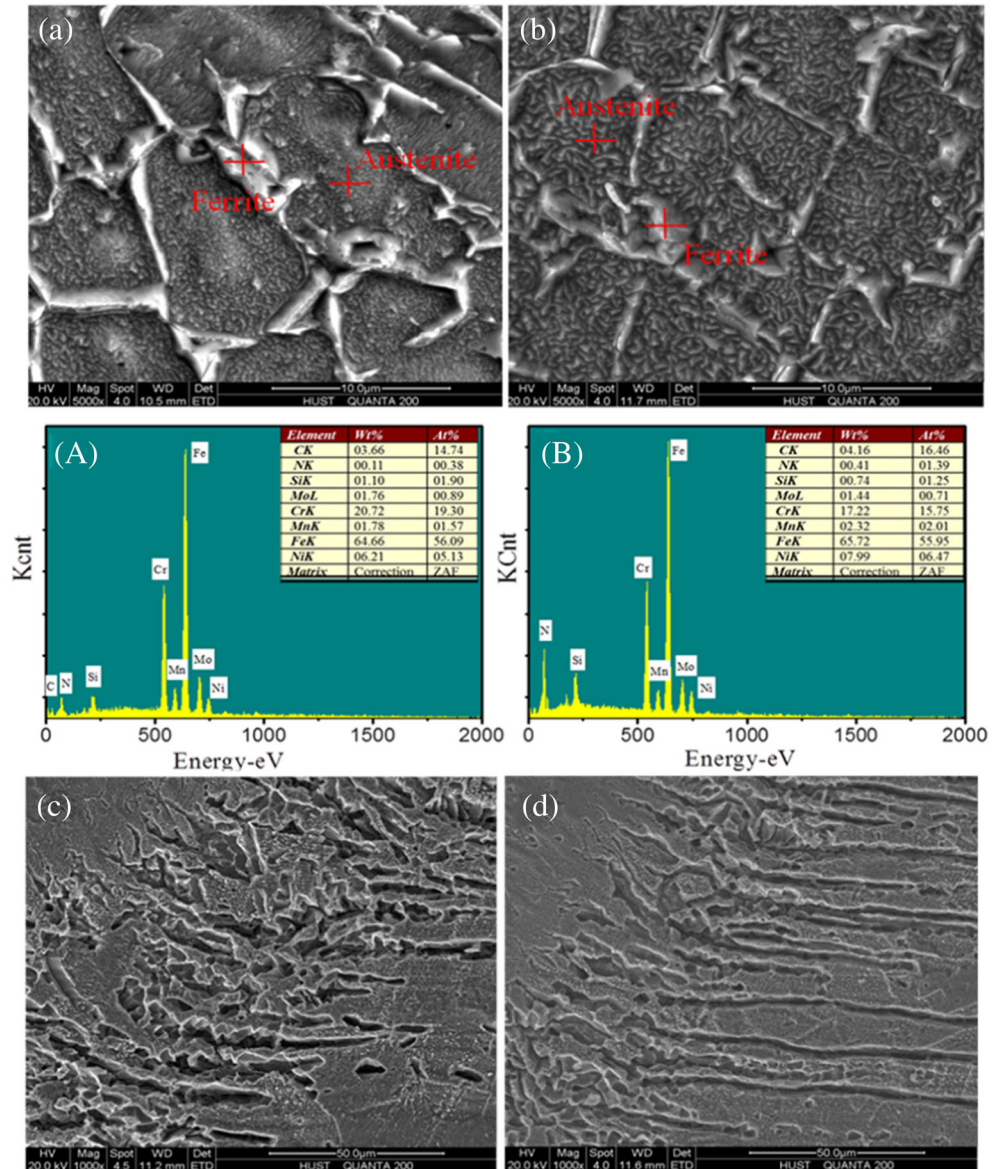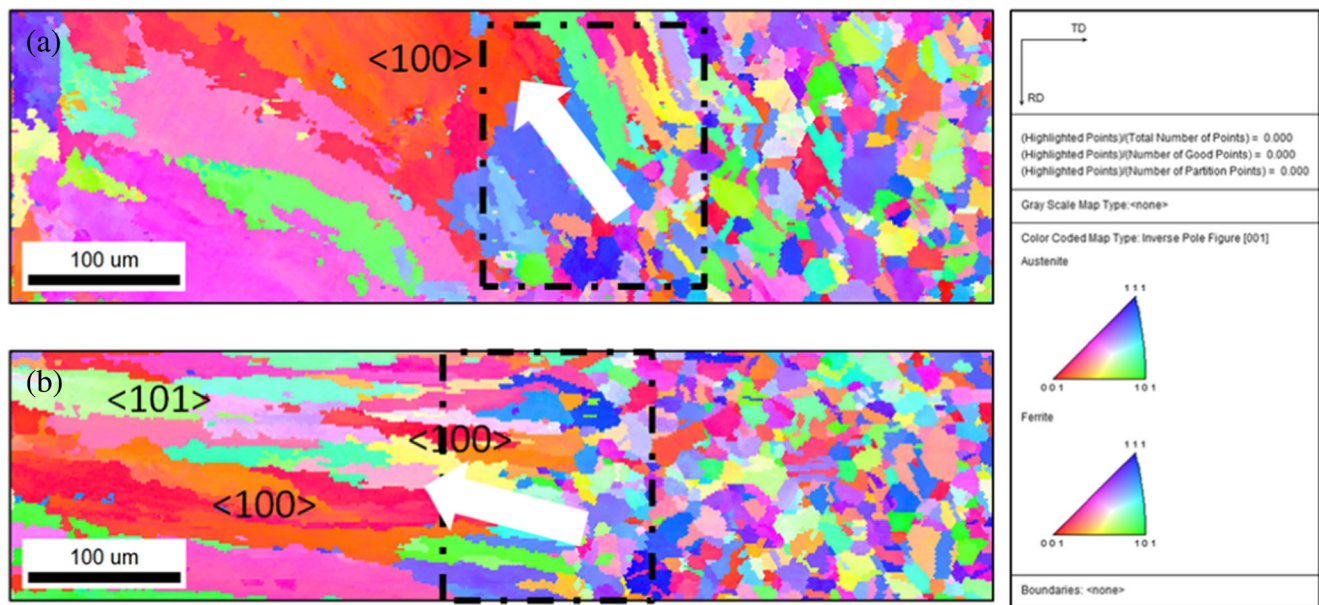
Fig. 5 EBSD images showing grain structures of welds **a** B = 0 mT and **b** B = 24 mT

through an electron universal testing machine, which is an equipment used to evaluate the mechanical properties of metallic materials.

Tensile test of each group was conducted three times. Load-elongation curves of the 0, 8, 16, and 24 mT samples are plotted in Fig. 7a. It is beneficial that no obvious yield phenomenon was observed during the tests. $A_0 = 40$ mm$^2$ represented original cross-sectional area at the fracture surface, and $L_0 = 50$ mm was the gauged length of the standard specimen. The stress $\sigma = F/A_0$ and elongation $\varepsilon = \Delta L/L_0$ were calculated considering $A_0$ and $L_0$ under the $F$-$\Delta L$ curve, and results were displayed in Fig. 7b. According to Fig. 7b, a tensile strength of 685.2 MPa was the average value for 0 mT samples. The highest average value of 765 MPa was observed for the 24 mT sample, of which the tensile strength improved by nearly 12%. The fracture morphologies of joints are shown in detail in Fig. 8 to investigate nature of the fracture. There were a large amount of porosities on the fracture surface. Comparing with Fig. 8a, porosities were much less in Fig. 8c.

### 3.5 Residual stress test

Figure 9a, b shows the residual stress as a function of the distance from the weld center. The measurements were conducted from the center of the weld zone (WZ) to one side of the HAZ perpendicular to the welding direction. The uncertainty during measurements was indicated by the error bar.

According to the results, the longitudinal and transverse residual stress of 0 mT samples were tensile stress in center of the WZ and compressive stress in HAZ, while the 24 mT sample had both compressive and tensile in the longitudinal plot. Besides, a remarkable drop occurred at interface of the WZ and HAZ, which was in consistence with results in [19]. According to the literature, this phenomenon was the consequence of differences in yield strength between the two zones. Considering the notable drop of residual stress, it was obvious that weld width was increased via the application of magnetic field. Additionally, the magnitude of residual stress in both directions for 24 mT sample was lower than 0 mT sample. The different cooling contractions and the phase transformation in weld would be responsible for the differences.
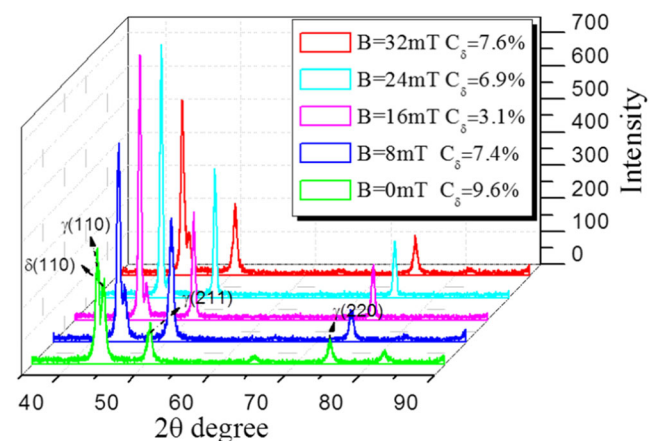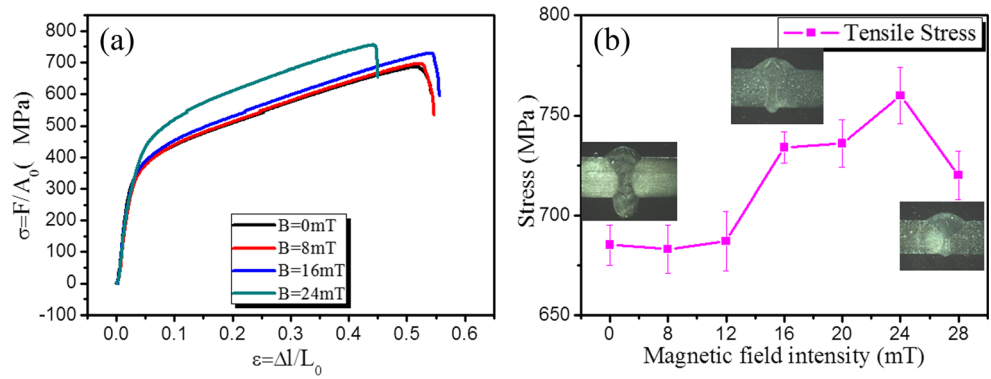


Fig. 6 XRD patterns of the welds

**Fig. 7** **a** The tensile test results of welded joints with 0, 8, 16, and 24 mT magnetic field. **b** Variations of ultimate tensile strength with external applied magnetic field intensity

## 3.6 Microhardness test

The distribution of microhardness is shown in Fig. 10. According to Fig. 10, widths of the WZ along line 1 were inconsistent with the geometry results in Fig. 3. The results showed that hardness in 0 mT sample was in an order of BM > WZ > HAZ. However, the hardness of WZ was nearly the same with those in HAZ for the 24 mT sample. It means that the distribution of microstructure became uniform in samples with an external magnetic field. Furthermore, the average microhardness values of WZ for 0 and 24 mT samples were 199.38 and 191.2 HV, respectively. The increasing of hardness in WZ with a magnetic field was attributed to the refining of the grains.

## 4 Discussion

### 4.1 Morphology and microstructure

In an attempt to figure out the improvements found in microstructure and mechanical properties, it is necessary to understand the synergistic effect between magnetic field and electric field in the molten pool. During the hybrid welding process with rectangle pulsed current, there appeared an inherent oscillating magnetic field in an annular direction in molten pool. As the external magnetic field of low intensity was applied perpendicular to the welding direction, there was an electromagnetic interaction that occurred between both magnetic fields which resulted in a stirring phenomenon within molten

**Fig. 8** Fracture morphology of the weld. **a**, **c** Porosity morphology in the fracture surface of 0 and 24 mT samples. **b**, **d** Dimples morphology of joints
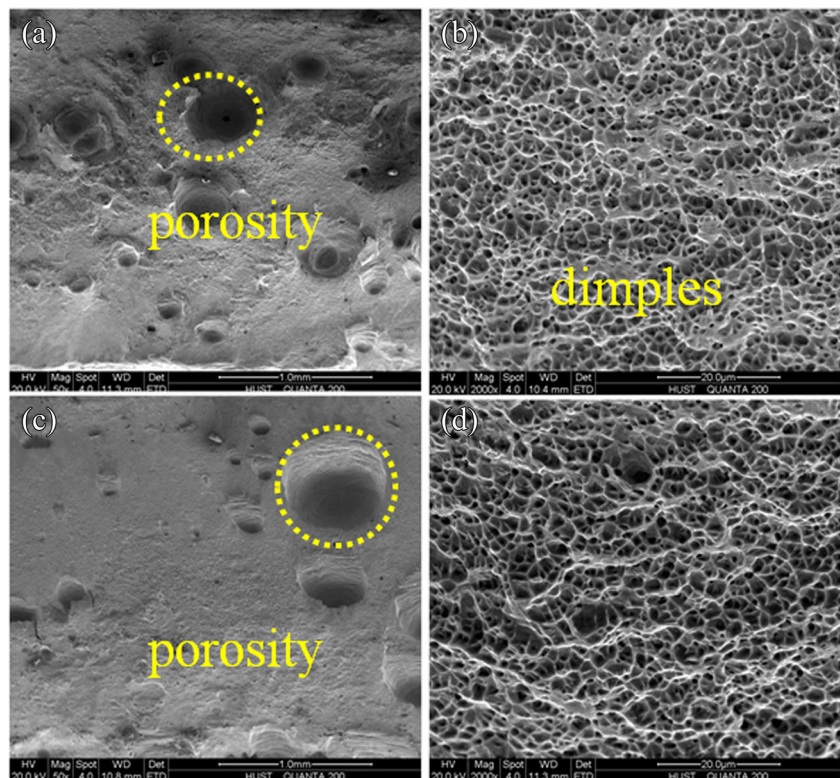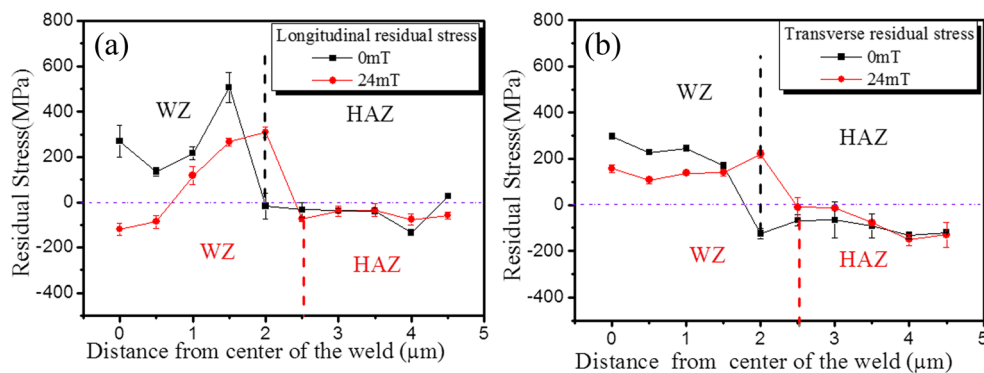
**Fig. 9** Distribution of residual stress. **a** Longitudinal and **b** transverse as functions of distance from center of the weld



pool. The flow field was changed through the stirring effect via the external magnetic field, which in turn gave a variation on the distribution of thermal field. The growth pattern and solidification microstructure were closely related to the thermal conditions in weld pool. Thus, the microstructures and mechanical properties were changed accordingly.

The weld was significantly increased in width. As for width changes of the arc area, some researchers had made some hypothesis. Malinowski-Brodnicka et al. [20] argued that the changes of the width in weld bead shape were results of arc rotation and annular flow of liquid weld metal in the weld pool during arc welding of austenitic stainless steel under magnetic field. Then, the assumption was confirmed by other groups by both experiments and simulations. As Zhang et al. [9] recorded behaviors of the arc and plasma under the magnetic field during hybrid welding, which revealed that the application of magnetic field changed the arc shape from pyramidal and static to spiral and rotational with a larger arc root diameter. Simulations by Wang et al. [21] showed that there existed significant spiral-shaped rotational phenomena in the magnetic field vacuum arcs. Therefore, it indicated that the increased width of samples were consequences of interaction between the magnetic field and the arc. Together with change of the arc shape, the other characteristics of the arc were varied correspondingly, such as distribution of the energy and temperature, temperature gradient along the arc axis, and the arc force in weld, and then resulted in variations in the weld flow and mechanical properties. The improved weld shape with decreased sagging metal was in accordance with the results by Shoichi et al. [22], which found that an axial magnetic field during the TIG welding could produce an upward electromagnetic force lifting the liquid metal up.

At the liquid-solid interface, new grains were nucleated and outgrew in an epitaxial mode and then grew into columnar grains competitively [23]. The preferential growth mode near the fusion line was explicitly displayed in results of the EBSD. It was reported by Campanella et al. [24] that grain refinement in casting with an external magnetic field were caused by melt stirring through two aspects: (1) Liquid flow penetrated into the solidified area and partially remelted the dendrite arms; (2)

thermal gradient in the liquid is lowered, which promoted the columnar to equiaxed transition. It was known that solidification and nucleation process in casting were similar to the conditions in welding; this refining mechanism was applicable in this case. However, as the average cooling rate was 4–100 °C/s, nearly $10^4$ bigger than speed of casting with $3 \times 10^{-4}$–$150 \times 10^{-4}$ °C/s [25], and the epitaxial growth was extensively appeared in weld pool, the effects were not as apparent as it appeared in casting and the refining effect mechanisms were not completely identical. The concept of dendrite fragmentation by an external magnetic field during the GTA welding was proposed in 1990 [20]; however, it had hardly been investigated in detail. The results in Fig. 5 revealed the mechanism of epitaxial and preferential growth, and the mechanism for the refining was indicated as well. According to the results in Fig. 5, the epitaxial grains were slightly finer in 24 mT sample than 0 mT sample; however, columnar grains in 24 mT sample were quite finer than in 0 mT sample. Grain in an optimum direction should grow into coarse columnar grains as it developed in Fig. 5a. However, some of the grains in <100> direction in Fig. 5b were supposed to be remelted by liquid flow or even detached from original position and then nucleated in other places; thus, the orientation changed into other directions, such as <101>. Not all the epitaxial grains in <100> direction developed into columnar grains; together with the refining grains grew from base metal, both of the
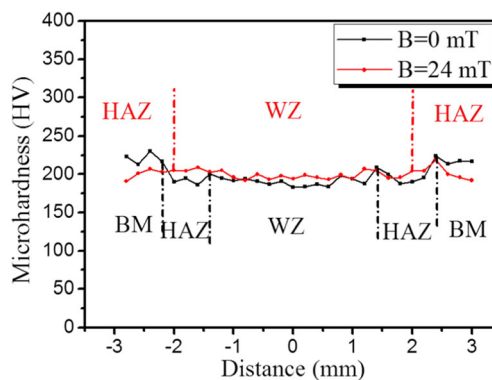


**Fig. 10** Distribution of microhardness across the welding zone for samples with different magnetic field intensity

factors led to the refining of grains. It was obviously found in the black rectangular boxes in Fig. 5.

Lee et al. [26] stated that the variation of the ferrite distribution in the austenite matrix affected the hot cracking and corrosion fatigue resistance. Thus, it was valuable to study the effect of the magnetic field on the phases in weld. Transformation of solid/solid was driven by the difference in the total Gibbs free energy $\Delta G_{total}$ of the two phases. It was also known that the saturation magnetizations of ferrite and austenite were quite different in a magnetic field. Garcin et al. [27] provided thermodynamic analysis that magnetic field exerted an effect during the solid/solid phase transformation of γ-δ for the magnetism of the parent phase, and the product phase is largely different. However, these effects on the driving force of transformation were only taken into action under a high-intensity magnetic field. In this case, the stirring effect caused by the interaction of induced oscillating magnetic field and external magnetic field played the dominant role. On the one hand, the stirring effect in weld promoted grains detachment and then generated an increment of sites for nucleation of γ-austenite. Thus, in the samples with an external magnetic field, process of δ → γ was promoted. As for the coarse ferrite in Fig. 4a, c, during the transformation of the longer δ → γ process in welding without a magnetic field, the ferrite was more likely to grow coarse. On the other hand, austenite was a paramagnetic phase, of which the domains were oriented randomly; thus, the interaction of the fields would induce vibration of the atoms [28]. The interaction on atoms vibration would also promote the transformation and then homogenized the matrix. Homogenizing of element distribution could also be confirmed by the microhardness profiles.

## 4.2 Mechanical properties

According to the results of tensile tests, the improvements of the ultimate tensile strength were significant with 16 and 24 mT magnetic field. The microsegregation and precipitation, as well as the porosity, were the most vulnerable area for the origin of the crack [18]. According to the enlarged morphologies in Fig. 8b, d, the surfaces were covered with fine and uniform dimples. It was inferred that the porosity formation was suppressed by the magnetic field, which could be convinced by the investigations in [29]. Results in the literature demonstrated that an external magnetic field force was proposed to control the back filling speed of liquid metal during the laser welding, by which the formation of porosity were suppressed. Furthermore, tensile strength was closely related with the elongated grains and grain sizes in weld [30]. As discussed above, elongated grains and finer ferrite in 24 mT sample exert an important influence on the improvements of tensile strength. Investigation by Haboudou et al. [31] proved that the change in thermal cycling could modify local hardness values by affecting the precipitations and phases. The refining

phenomenon contributed to the increase of hardness in WZ and HAZ as well. Another factor taken into consideration for influencing the microhardness was the suppression of the porosity formation.

Even though the maximum tensile stresses in weld were lower than the ultimate tensile strength of the base metal, it could lead to a premature failure during the service life. It is known that high tensile residual stresses would produce severe effect on mechanical property [30]. It was revealed that the distributions of residual stresses are combination results of volume variation induced by phase transformation and heterogeneous thermal strains induced by the thermal gradients [32]. Based on this mechanism, the residual stresses distributed in WZ and HAZ were simulated and explained in the literatures [33, 34]. In this case, the decrease of residual stress in 24 mT samples can be attributed to the homogeneous grains distribution caused by the stirring effect via the external magnetic field. Moreover, the homogeneous microstructure can also be confirmed through the stabilized microhardness in WZ samples with a magnetic field in Fig. 10. On the other hand, as the γ-austenite was face-centered cubic crystal and δ-ferrite was body-centered cubic crystal, the crystal lattice was shrunk during transformation from δ to γ for the different compactness. The extra volume released from the transformation would contribute to the decreased of residual stress. Considering the results in Fig. 7, the transformation was promoted with an external magnetic field; thus, the magnitude of residual stress for 24 mT sample was lower than 0 mT sample. It is known that pronounced tensile residual stresses in the longitudinal direction are generated in center of the weld as the results obtained in 0 mT sample, while the 24 mT sample has both compressive and tensile in the longitudinal plot, which could be explained in terms of two points: one for the increased weld width; another was the variation of flow mode in molten pool brought by external magnetic field. Nevertheless, further experiments and analysis are still needed to give an accurate interpretation.

## 5 Conclusions

In this study, it was proved that an appropriate magnitude of magnetic field changed the microstructure and improved mechanical properties of the joints. As this was a process mode full of flexibility, it is proved to be a suitable choice to improve the laser-MIG hybrid welding process. Effects of the static magnetic field during laser-arc hybrid welding were summarized in detail as follows:

(1) Stirring effect caused by the interaction of internal induced magnetic field and external magnetic field led to refined grains and uniformity of element distribution. Nucleation rate was increased as well, which promoted

the $\delta$-$\gamma$ transformation then resulted in a decreased volume of ferrite.

(2) Tensile strength was improved by an appropriate magnitude magnetic field, of which improved by 12% with a 24-mT magnetic field.

(3) Compared with samples without magnetic field, residual stresses were lower and microhardness of the weld with magnetic field was higher and more uniform.

# References

1. Asai S (1989) Electromagnetic processing of materials. Zairyo to Purosesu (Current Advances in Materials and Processes), pp 205–206.

2. Bachmann M, Avilov V, Gumenyuk A, Rethmeier M (2014) Experimental and numerical investigation of an electromagnetic weld pool control for laser beam welding. Phys Procedia 56:515–524. doi:10.1016/j.phpro.2014.08.006

3. Liu Y, Sun Q, Liu J, Wang S, Feng J (2015) Effect of axial external magnetic field on cold metal transfer welds of aluminum alloy and stainless steel. Mater Lett 152:29–31. doi:10.1016/j.matlet.2015.03.077

4. Tse HC, Man HC, Yue TM (1999) Effect of magnetic field on plasma control during $CO_2$ laser welding. Optics Laser Technol 31:363–368. doi:10.1016/S0030-3992(99)00080-8

5. Tse HC, Man HC, Yue TM (1999) Effect of electric and magnetic fields on plasma control during $CO_2$ laser welding. Opt Laser Eng 32:55–63. doi:10.1016/S0143-8166(99)00045-7

6. Bachmann M, Avilov V, Gumenyuk A, Rethmeier M (2014) Experimental and numerical investigation of an electromagnetic weld pool support system for high power laser beam welding of austenitic stainless steel. J Mater Process Tech 214:578–591. doi:10.1016/j.jmatprotec.2013.11.013

7. Mousavi MG, Hermans MJM, Richardson IM, Den Ouden G (2003) Grain refinement due to grain detachment in electromagnetically stirred AA7020 welds. Sci Technol Weld Joi 8:309–312. doi:10.1179/136217103225005462

8. Bachmann M, Avilov V, Gumenyuk A, Rethmeier M (2014) About the influence of a steady magnetic field on weld pool dynamics in partial penetration high power laser beam welding of thick aluminium parts. Int J Heat Mass Tran 60:309–321. doi:10.1016/j.ijheatmasstransfer.2013.01.015

9. Zhang X, Zhao ZY, Wang CM, Yan F, Hu XY (2015) The effect of external longitudinal magnetic field on laser-MIG hybrid welding. Int J Adv Manuf Technol 85:1735–1173. doi:10.1007/s00170-015-8035-9

10. Liu S, Li Y, Liu F (2016) Effects of relative positioning of energy sources on weld integrity for hybrid laser arc welding. Opt Laser Eng 81:87–96. doi:10.1016/j.optlaseng.2016.01.010

11. Stute U, Kling R, Hermsdorf J (2007) Interaction between electrical arc and Nd: YAG laser radiation. CIRP Annals-Manuf Techn 56:197–200. doi:10.1016/j.cirp.2007.05.048

12. He C, Huang C, Liu Y (2015) Effects of mechanical heterogeneity on the tensile and fatigue behaviours in a laser-arc hybrid welded aluminium alloy joint. Mater Design 65:289–296. doi:10.1016/j.matdes.2014.08.050

13. Bagger C, Olsen FO (2005) Review of laser hybrid welding. J Laser Appl 17:2–14. doi:10.2351/1.1848532

14. Liu T, Yan F, Liu S, Li R, Wang C, Hu X (2016) Microstructure and mechanical properties of laser-arc hybrid welding joint of GH909 alloy. Optical Laser Technol 80:56–66. doi:10.1016/j.optlastec.2015.12.020

15. Ruud CO (1982) A review of selected non-destructive methods for residual stress measurement. NDT Int 15:15–23. doi:10.1016/0308-9126(82)90083-9

16. Standard, ASTM (2003, November) Standard practice for x-ray determination of retained austenite in steel with near random crystallographic orientation. American Society for Testing and Materials

17. Jatczak CF (1980) Retained austenite and its measurement by x-ray diffraction (No. 800426). SAE Technical Paper. doi: 10.4271/800426

18. Molak RM, Paradowski K, Brynk T, Ciupinski L, Pakiela Z, Kurzydlowski KJ (2009) Measurement of mechanical properties in a 316 L stainless steel welded joint. Int J Pres Ves Pip 86:43–47. doi:10.1016/j.ijpvp.2008.11.002

19. Lee CH, Chang KH (2012) Temperature fields and residual stress distributions in dissimilar steel butt welds between carbon and stainless steels. Appl Therm Eng 45:33–41. doi:10.1016/j.applthermaleng.2012.04.007

20. Malinowski-Brodnicka M, Den Ouden G, Vink WJP (1990) Effect of electromagnetic stirring on GTA welds in austenitic stainless steel. Weld J 2:52s–59s

21. Wang L, Jia S, Zhou X (2012) Three-dimensional model and simulation of vacuum arcs under axial magnetic fields. Phys Plasmas (1994-present) 19:013507. doi:10.1063/1.3677881

22. Shoichi M, Yukio M, Koki T (2013) Study on the application for electromagnetic controlled molten pool welding process in overhead and flat position welding. Sci Technol Weld Joi 18:8–44. doi:10.1179/1362171812Y.0000000070

23. Sundaresan S, Ram GDJ (1999) Use of magnetic arc oscillation for grain refinement of gas tungsten arc welds in $\alpha$–$\beta$ titanium alloys. Sci Technol Weld Joi 4:151–160. doi:10.1179/136217199101537699

24. Campanella T, Charbon C, Rappaz M (2004) Grain refinement induced by electromagnetic stirring: a dendrite fragmentation criterion. Metall Mater Trans A 35:3201–3210. doi:10.1007/s11661-004-0064-1

25. Wu SS, Liu YQ (2011) Material forming principle. China Machine Press, Beijing

26. Lee JS, Fushimi K, Nakanishi T, Hasegawa Y, Park YS (2014) Corrosion behaviour of ferrite and austenite phases on super duplex stainless steel in a modified green-death solution. Corros Sci 89:111–117. doi:10.1016/j.corsci.2014.08.014

27. Garcin T, Rivoirard S, Elgoyhen C, Beaugnon E (2010) Experimental evidence and thermodynamics analysis of high magnetic field effects on the austenite to ferrite transformation temperature in Fe–C–Mn alloys. Acta Mater 58:2026–2032. doi:10.1016/j.actamat.2009.11.045

28. Curiel FF, García R, López VH (2011) Effect of magnetic field applied during gas metal arc welding on the resistance to localised corrosion of the heat affected zone in AISI 304 stainless steel. Corros Sci 53:2393–2399. doi:10.1016/j.corsci.2011.03.022

29. Zhou J, Tsai HL (2007) Effects of electromagnetic force on melt flow and porosity prevention in pulsed laser keyhole welding. Int J Heat Mass Tran 50:2217–2235. doi:10.1016/j.ijheatmasstransfer.2006.10.040

30. Zhang L, Lu JZ, Luo KY (2013) Residual stress, micro-hardness and tensile properties of ANSI 304 stainless steel thick sheet by fiber laser welding. Mat Sci Eng: A 561:136–144. doi:10.1016/j.msea.2012.11.001

31. Haboudou A, Peyre P, Vannes AB (2003) Reduction of porosity content generated during Nd: YAG laser welding of A356 and AA5083 aluminium alloys. Mat Sci Eng: A 363:40–52. doi:10.1016/S0921-5093(03)00637-3

32. Mehdi B, Badji R, Ji V (2016) Microstructure and residual stresses in Ti-6Al-4V alloy pulsed and unpulsed TIG welds. J Mater Process Tech 231:441–448. doi:10.1016/j.jmatprotec.2016.01.018

33. Casavola C, Pappalettere C, Tattoli F (2012) Residual stresses and fatigue behavior of hybrid butt welded joints. NT2F12:169–186

34. Longuet A, Robert Y, Aeby-Gautier E (2009) A multiphase mechanical model for Ti–6Al–4V: application to the modeling of laser assisted processing. Comp Mater Sci 46:761–766. doi:10.1016/j.commatsci.2009.05.012